Geosci. Model Dev., 18, 8569–8587, 2025 https://doi.org/10.5194/gmd-18-8569-2025 © Author(s) 2025. This work is distributed under the Creative Commons Attribution 4.0 License.





All-sky AMSU-A radiance data assimilation using the gain-form of Local Ensemble Transform Kalman filter within MPAS-JEDI-2.1.0: implementation, tuning, and evaluation

 $Tao\ Sun^1$, Jonathan J. Guerrette 1,a , Zhiquan Liu^1 , Junmei Ban^1 , Byoung-Joo $Jung^1$, Ivette Hernandez $Banos^1$, and $Chris\ Snyder^1$

¹NSF National Center for Atmospheric Research, Boulder, CO 80301, USA

Correspondence: Tao Sun (taosun@ucar.edu)

Received: 5 May 2025 - Discussion started: 15 May 2025

Revised: 9 October 2025 – Accepted: 11 October 2025 – Published: 14 November 2025

Abstract. The Gain-form of Local Ensemble Transform Kalman Filter (LGETKF) has been implemented in the Joint Effort for Data assimilation Integration (JEDI) with the Model for Prediction Across Scales - Atmosphere (MPAS-A) (i.e., MPAS-JEDI). LGETKF applies vertical localization in model space and is particularly convenient for assimilating satellite radiances that do not have an explicit vertical height assigned to each channel. Additional efforts are made to optimize the ensemble analysis procedure and improve the computational efficiency of MPAS-JEDI's LGETKF. This is the first application of JEDI-based LGETKF for assimilating radiance data in all-weather situations with a global MPAS configuration. The system is first tuned for covariance inflation and horizontal localization settings. It is found that using a combination of relaxation to prior perturbation (RTPP) and relaxation to prior spread (RTPS) outperforms using RTPP or RTPS alone, and using a smaller horizontal localization scale for all-sky radiances is preferable. With the optimized inflation and localization settings, assimilating all-sky radiances of the Advanced Microwave Sounding Unit – A (AMSU-A) window channels with an 80-member LGETKF improved the forecasts of moisture, wind, clouds, and precipitation fields, when compared to the benchmark experiment without assimilation of all-sky AMSU-A radiances. The positive forecast impact of all-sky AMSU-A radiances is the largest over the tropical regions up to 7 d. Some degradation in the temperature forecasts is seen over certain regions, where the model forecast is likely biased, causing deficiencies for assimilating all-sky data. The LGETKF capability is available

in the recent public release of MPAS-JEDI and is ready for research and operational explorations.

1 Introduction

The Joint Effort for Data assimilation Integration (JEDI) is a new data assimilation (DA) framework with modelagnostic components that can be interfaced to multiple models (Trémolet and Auligné, 2020). The development of JEDI is led by the Joint Center for Satellite Data Assimilation (JCSDA) with partners from several research and operational institutes. Considerable efforts at the National Center for Atmospheric Research (NCAR) have been devoted to the development of a JEDI-based DA system for the Model for Prediction Across Scales - Atmosphere (MPAS-A; Skamarock et al., 2012), which we will call MPAS-JEDI. (For historical reasons, this system has been previously referred to as JEDI-MPAS, such as in Liu et al., 2022.) Variational DA approaches have been successfully implemented into MPAS-JEDI for deterministic analysis, including the three-dimensional variational (3DVar) method, the ensemble-variational (EnVar) method, and hybrid variants of EnVar (Liu et al., 2022; Jung et al., 2024).

Ensemble DA plays a vital role in numerical weather prediction (NWP) by providing initial conditions for ensemble forecasts, which can also be used as input for deterministic EnVar analyses to form flow-dependent background error covariances (BECs). There are two general classes of ensem-

^anow at: Tomorrow.io, Golden, CO 80401, USA

ble DA methods, the ensemble of data assimilations (EDA; Houtekamer et al., 1996) and various versions of the Ensemble Kalman Filter (EnKF; Evensen, 2003). For MPAS-JEDI, Guerrette et al. (2023) implemented EDA that performs an ensemble of 3DEnVar analysis with perturbed observations. They demonstrated a comparable or superior performance for EDA when compared to the Ensemble Adjustment Kalman Filter (EAKF; Anderson, 2001) within the Data Assimilation of Research Testbed (DART; Anderson et al., 2009; Ha et al., 2017), but with a substantially larger computational cost than the EAKF. Therefore, it is worth implementing an EnKF-based ensemble DA capability for MPAS-JEDI.

Frolov et al. (2024) implemented two EnKF-based methods within the JEDI framework, including the Local Ensemble Transform Kalman Filter (LETKF; Hunt et al., 2007) and the gain-form LETKF (LGETKF; Bishop et al., 2017). Frolov et al. (2024) provided a comprehensive description of both methods and demonstrated their successful application to different components of the Earth system model. Park et al. (2023) showed that the limited-area FV3-JEDI's LETKF and LGETKF have a comparable performance in the convective-scale radar DA when compared to the Ensemble Square Root Filter (EnSRF; Whitaker and Hamill, 2002; Tippett and Anderson, 2003) in the Gridpoint Statistical Interpolation (GSI; Shao et al., 2016) DA system. Compared to the LETKF, the LGETKF has the advantage in performing vertical localization in model space (Bishop et al., 2017), making it particularly suitable for the assimilation of satellite radiances that are column-integrated measurements and are hard to define their vertical coordinates. Various studies have proven that the model space vertical localization generally outperforms observation space vertical localization (Campbell et al., 2010; Bishop et al., 2017; Lei et al., 2018). Given the feasibility of the LGETKF algorithm within the JEDI framework, implementing it to MPAS-JEDI is a worthwhile endeavour, as it better handles the vertical localization of satellite radiance assimilation.

The cloud- and precipitation-affected satellite radiances from microwave (MW) instruments have been operationally assimilated in the global NWP models in recent decades (e.g., Bauer et al., 2010; Zhu et al., 2016, 2019; Geer et al., 2017, 2018; Migliorini and Candy, 2019; Shahabadi and Buehner, 2024) with the variational-based DA systems. EnKF-based methods were also employed to assimilate allsky infrared radiances for case studies with regional models (e.g., Zhang et al., 2016; Minamide and Zhang, 2018; Honda et al., 2018; Zhang et al., 2019; Okamoto et al., 2019; Chan et al., 2020; Zhu et al., 2023). Fewer studies, however, have explored all-sky assimilation of MW radiances using EnKFbased methods for global models. Bonavita et al. (2020) presented a comprehensive evaluation of the all-sky MW radiance assimilation with the European Centre for Medium-Range Weather Forecasts (ECMWF)'s EnKF system, and their results showed that EnKF could properly extract wind information from all-sky radiance observations and brings 2 %–4 % improvement in forecast scores.

In this study, the LGETKF algorithm within the JEDI framework is implemented in MPAS-JEDI, and its performance is evaluated through the clear-sky and all-sky MW radiance assimilation. As the first implementation of LGETKF in MPAS-JEDI, we first tune the assimilation configurations such as covariance inflation and localization, providing a reference for the community on achieving stable and robust performance. We then assess the forecast impact of all-sky assimilation of AMSU-A radiances over a month-long period, offering deeper insight into the performance of MPAS-JEDI's LGETKF. The rest of the paper is organized as follows. In Sect. 2, the implementation of the LGETKF in MPAS-JEDI is detailed. The MPAS model configuration, allsky radiance DA method, and experimental design are provided in Sect. 3. The results of tuning the covariance inflation and horizontal localization are given in Sect. 4, followed by our evaluation of all-sky AMSU-A radiance DA with the LGETKF in Sect. 5 and conclusions in Sect. 6.

2 Methodology

2.1 LGETKF in MPAS-JEDI

2.1.1 Implementation of LGETKF in MPAS-JEDI

The local volume solvers developed by Frolov et al. (2024), which are part of the Object-Oriented Prediction System (OOPS), the DA solver component of JEDI, have been implemented in MPAS-JEDI. Both the LETKF and LGETKF are now available in MPAS-JEDI, with the latter being the focus of this study. In the LGETKF, the model states within a local volume (i.e., a vertical column of a horizontal grid point) are updated using the surrounding observations, and the updates in each volume occur simultaneously and independently from other volumes. When computing the Kalman gain, the LGETKF employs perturbations from an expanded ensemble, which is obtained by modulating the original ensemble with the eigenvectors of the vertical localization matrix (Bishop et al., 2017). Thus, the LGETKF has the advantage of performing vertical localization in model space and is particularly suitable for assimilating non-local observations such as satellite radiances (Lei et al., 2018). For a detailed description of the LGETKF algorithm within OOPS, see Frolov et al. (2024).

The analysis variables of MPAS-JEDI's LGETKF include temperature (T), horizontal wind components (U, V), surface pressure (P_s) , and specific humidity (Q). For all-sky radiance assimilation, additional five hydrometeor analysis variables are introduced: the mixing ratios of cloud water (Q_c) , cloud ice (Q_i) , rainwater (Q_r) , snow (Q_s) , and graupel (Q_g) . Following Guerrette et al. (2023) and Jung et al. (2024), linearized hydrostatic balance constraint is

used when computing increments of dry-air density (ρ_d) and three-dimensional pressure (P) from the increments of T, Q, and P_s . After the ensemble update, the analysis variables are transformed to MPAS-A's prognostic variables.

2.1.2 Covariance inflation

There are three multiplicative covariance inflation schemes available within JEDI, including one prior inflation scheme and two posterior inflation schemes with the relaxation to prior perturbation (RTPP; Zhang et al., 2004) and the relaxation to prior spread (RTPS; Whitaker and Hamill, 2012).

The prior inflation scheme multiplies the background error covariance by a factor $\alpha > 1$:

$$\mathbf{X}_{\text{inf}}^{\text{b}}(\mathbf{X}_{\text{inf}}^{\text{b}})^{\text{T}} = \alpha \mathbf{X}_{\text{pri}}^{\text{b}}(\mathbf{X}_{\text{pri}}^{\text{b}})^{\text{T}}, \tag{1}$$

where **X** is the matrix whose columns are deviation of the ensemble members from the ensemble mean, and the subscript pri and inf denote prior (i.e., before inflation) and inflated, respectively. The RTPP scheme blends the background and analysis ensemble perturbations as

$$\mathbf{X}_{\text{inf}}^{a} = \alpha_{\text{rtpp}} \mathbf{X}^{b} + (1 - \alpha_{\text{rtpp}}) \mathbf{X}^{a}, \tag{2}$$

where superscripts a and b denote analysis and background quantities, and α_{rtpp} denotes the relaxation parameter of RTPP. In the RTPS scheme, the analysis perturbations are inflated as

$$\mathbf{X}_{\text{inf}}^{\mathbf{a}(i)} = \left(\frac{\alpha_{\text{rtps}}\sigma^{\mathbf{b}(i)} + (1 - \alpha_{\text{rtps}})\sigma^{\mathbf{a}(i)}}{\sigma^{\mathbf{a}(i)}}\right) \mathbf{X}^{\mathbf{a}(i)},\tag{3}$$

where α_{rtps} is the relaxation parameter of RTPS, the superscript (i) indicates a quantity relevant to the ith element of the state vector \mathbf{x} , and σ is the ensemble spread. The inflation parameter α in both RTPP and RTPS is between 0 and 1, where $\alpha=0$ indicates no inflation and $\alpha=1$ corresponds to relaxing to the background ensemble spread. Within MPASJEDI's LGETKF, the three inflation schemes can be employed either individually or in various combinations. Posterior inflation is used in this study.

2.1.3 Covariance localization

The R-localization approach (Hunt et al., 2007) is employed for the observation-space horizontal localization in LGETKF. In this approach, the observation error covariance, **R**, is inflated as a function of the distance between the analysed local volume and surrounding observation locations. The localization is typically performed by multiplying the inverse of a correlation-like function, such as Box Car, Gaspari-Cohn (Gaspari and Cohn, 1999), or the second order auto regressive (SOAR), to the diagonal elements of **R**. Consequently, the influence of observations to the state variables within a local volume decreases smoothly with increasing distance, and observations beyond the specified horizontal localization scale have no influence on the model state update. To speed up the horizontal localization operation, only a

limited number of observations (e.g., 1000 used in this study) closest to a local volume is included in the horizontal localization. Additionally, different horizontal localization scales can be applied for different observation types.

The vertical localization in LGETKF is done in model space through the modulated ensemble members it introduces. There are several vertical coordinate options available for vertical localization, including the model level, height, and scale height ($\log(P)$). To reduce the computational cost, it is a common practice, when constructing the modulated ensemble, to approximate the vertical localization matrix using only its first several dominant eigenvectors. In this study, we retain 11 eigenvectors (and thus 11 modulated members for each original ensemble member), which explain $\sim 95\,\%$ of the variance of our chosen Gaspari-Cohn localization matrix with a 6 km scale.

2.2 LGETKF analysis procedure

As shown in Fig. 1, the LGETKF analysis procedure is split into three steps: the Observer step for the ensemble background, the Solver step for ensemble update, and the Observer step for ensemble analysis. In the Observer step for the ensemble background (denoted "OMB"), the model equivalent of the observations (hereafter HofX) is computed for both the original ensemble background members and their corresponding modulated members and then written out into separate files for each ensemble member. The OMB step is carried out with multiple simultaneous jobs, in which the HofX application is looping for a trunk of original and modulated members. The Solver step with a single job then reads in the outputs from the OMB step to solve the LGETKF, generating ensemble analysis members. In the Observer step for the ensemble analysis (denoted as "OMA"), HofX calculations are performed solely for the original analysis members, omitting the modulated members. Both OMB and OMA steps employ the "Round robin" observation distribution, ensuring an effective load balancing of observations across parallel processing elements (PEs). The "Halo" observation distribution must be utilized in the Solver step, storing overlapping sets of observations on each PE and eliminating the need for inter-PE communications by ensuring all required observations for updating model states within a PE available locally. More details on "Round robin" and "Halo" can refer to Frolov et al. (2024).

Note that the OMB and Solver steps can be configured to run within a single job execution. In that case, the OMB step must also use the "Halo" distribution and the HofX applications for all original and modulated members will have to be run one by one, which leads to a much longer time-to-completion of LGETKF, when compared to the separate job strategy described above. The observation count is another important factor for the memory use and computational speed of both the Observer and Solver steps. To further improve the computational efficiency, a quality control

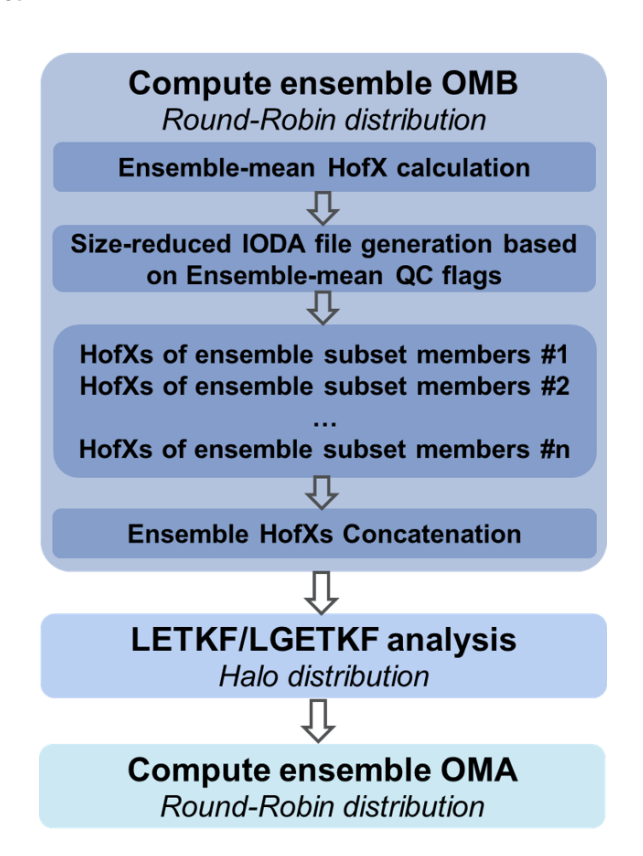


Figure 1. Flow chart of the analysis procedure of LGETKF.

(QC) step applying HofX to the ensemble mean background is run before the ensemble OMB step. This QC step writes out HofX files (one file for one observation type) with QC flags indicating bad and thinned observations, and then an offline program reads these HofX files and writes out new size-reduced observation files by excluding observations that fail QC or are not used after data thinning. The smaller observation files are then used in the subsequent OMB, Solver, and OMA steps. Note that the OMA step is mainly for analysis diagnostics, e.g., comparing the analysis fit to observations with the background fit to observations. Therefore, the ensemble forecast step for proceeding to the next cycle can begin before launching the OMA step. Recently, a new function named "reduce obs space" has been introduced in UFO. This function filters out observations that fail pre-processing checks (e.g., thinning, domain checks) directly in memory during runtime, avoiding unnecessary HofX calculation and storage. Its application is worth exploring as a way to eliminate the separate QC step in the current workflow. In addition, the linear operator is now available for computing ensemble HofXs, following Lei et al. (2018), which is expected to significantly accelerate the Observer step.

The 80-member MPAS-JEDI's LGETKF experiments configured with a global quasi-uniform grid spacing of 60 km (see Sect. 3) are conducted on the NCAR's supercomputer Derecho. Table 1 summarizes the wall-clock times of the

three job steps of LGETKF at the first analysis time. The QC step, involving HofX of the ensemble-mean background and the processing of more than 3 million observations, takes about 5.5 minutes when using 4 nodes and 128 cores per node. For each ensemble member, the OMB step consists of HofXs of that background member and its 11 modulated members for the remaining 563 197 observations; these calculations need about 5 min when using a single node. The Solver step updating all 80 members together takes about 25 min when using 12 nodes and 64 cores per node. Without these modifications to the analysis procedure, the OMB step takes over 90 min to finish the calculation of HofXs for all members and their modulated members, and the Solver step takes about 32 min due to the larger observation file read-in. This demonstrates the effectiveness of the improved analysis procedure in MPAS-JEDI's LGETKF. However, the Solver step remains relatively slow and may be not yet feasible for potential operational applications. While using more processors could reduce the run time, the increasing I/O burden for reading observation files limits the achievable performance gains. Active development is ongoing to further improve the computational efficiency of JEDI in general and we anticipate that the time-to-completion of MPAS-JEDI's LGETKF will be further reduced in future versions.

3 MPAS-A model configuration, observations, and experimental design

3.1 MPAS-A model configuration

A modified version of MPAS-A version 7.1 is employed as the NWP model in this study, similar to that used by Liu et al. (2022). MPAS-A is a non-hydrostatic model, which is discretized on an unstructured centroidal Voronoi horizontal mesh with C-grid staggering of the state variables for both global and regional applications (Skamarock et al., 2012, 2018). The quasi-uniform global mesh at a grid spacing of $\sim 60 \, \mathrm{km}$ is used in this study with 163 842 horizontal cells, 55 vertical levels, and a model top height of 30 km. The time step is 360 s. The "mesoscale reference" suite is employed for physical parameterizations, utilizing the parameterization schemes detailed in Table 2 in Liu et al. (2022).

3.2 Observations

A variety of observations are assimilated in this study, including radiosondes (temperature, zonal and meridional wind components, specific humidity), aircraft (temperature, zonal and meridional wind components, specific humidity), surface pressure, satellite-derived atmospheric motion vectors (AMV; zonal and meridional wind components), Global Navigation Satellite System Radio Occultation (GNSS RO) bending angle, as well as satellite radiances of selected channels from the Advanced Microwave Sounding Unit-A (AMSUA-A) and Microwave Humidity Sounder (MHS). Use

Key steps of Nodes/ Wall-clock Total number of cores per code Time obs. locations 344 s3 087 116 QC step 4/128 OMB step for one original and eleven modulated members 286 s563 197 1/128 Solver step 12/64 1470 s 563 197

Table 1. Computational resources for different steps of LGETKF at 00:00 UTC 15 April 2018.

of GNSS RO bending angle instead of refractivity is a common practice at operational centres (Healy and Thépaut, 2006; Rennie, 2010; Cucurull et al., 2013) and improves on the assimilation of refractivity that was employed in previous MPAS-JEDI studies (Ivette, personal communication 2024). All experiments assimilate clear-sky AMSU-A radiances from six satellites (NOAA-15/18/19, Aqua, Metop-A/B) and clear-sky MHS radiances from 4 satellites (NOAA-18/19, Metop-A/B). In addition, AMSU-A window-channel radiances from five satellites are assimilated over the water using the all-sky approach in the all-sky radiance DA experiments. The assimilated clear-sky and all-sky channels for different sensors and satellites are summarized in Table 2.

The experiments of Liu et al. (2022), Guerrette et al. (2023), and Jung et al. (2024) assimilated observations that were taken from so-called "GSI-ncdiag" files and had been pre-processed by the GSI DA system, including QC, radiance thinning, and radiance bias correction. Here, we begin from the raw observations (except for MHS radiances) and perform QC, observation error modelling, and bias correction of satellite radiances within MPAS-JEDI using the functions from JEDI's Unified Forward Operators (UFO) configured to mimic the QC procedures in GSI. The MHS satellite radiance observations are still taken from the GSI-ncdiag files, but the bias correction is done within MPAS-JEDI. Observations are converted to IODA from their native format using obs2ioda (https://github.com/NCAR/obs2ioda, last access: 17 October 2025).

3.2.1 Quality control

For all observations, the "PreQC" and "Background Check" filters are applied. The "PreQC" filter discards observations whose "PreQC" quality flags (provided in the observation conversion step for most observations or by GSI for MHS radiance data) are greater than zero for radiance data and 3 for other types of observations. The "Background Check" is employed to reject the observations whose absolute departure from the background exceeds three times the observation error standard deviation. For the surface pressure, a terrain correction scheme (Ingleby, 2014) is applied to correct the model-diagnosed surface pressure to the height of the surface station, and an additional QC is applied to reject observations where the differences between surface station height and model terrain height exceed 200 m. GNSS RO bending angle observations are only assimilated below

the 30 km model top and use height- and regionally dependent error variances estimated within UFO via the method of Desroziers et al. (2005). Satellite radiances and AMVs are thinned to 145 km spacing to reduce the spatial correlations. Following Guerrette et al. (2023), the observation errors of satellite AMVs are height dependent.

Quality control for clear-sky AMSU-A radiances follows Zhu et al. (2016). First, the cloud liquid water (CLW) content is retrieved from AMSU-A channels 1 and 2, following Grody et al. (2001). Pixels with CLW contents exceeding 0 kg m⁻² are excluded in channels 5 and 6. Next, a thick-cloud filter is applied to remove radiances affected by thick clouds, which are identified through the differences between observations and background in both CLW and radiances. Finally, radiances affected by precipitation are identified and filtered out using the scattering index (Grody et al., 1999). More details of AMSU-A quality control procedures can be found in Zhu et al. (2016).

3.2.2 Radiance bias correction

The radiance bias b of each channel at different locations is modelled within UFO as a weighed sum of predictors:

$$b = \beta_0 + \sum_{k=1}^K \beta_k p_k,\tag{4}$$

where β_0 is the constant offset, p_k the kth predictor, and β_k the corresponding bias correction coefficient. The bias predictors used in this study are the temperature lapse rate and its square, surface emissivity, and sensor scan angle and its second, third, and fourth powers. In this study, the bias correction coefficients at each LGETKF analysis cycle are obtained from an existing 1-month cycling hybrid-3DEnVar experiment, in which the bias correction coefficients are updated across the DA cycles with the variational bias correction (VarBC; Dee and Uppala, 2009) technique.

3.2.3 All-sky radiance assimilation

The LGETKF of MPAS-JEDI has the capability of assimilating radiances using the all-sky approach, following the same procedures described by Liu et al. (2022) for MPAS-JEDI's variational DA methods. Three key ingredients for all-sky radiance DA include the introduction of hydrometeors as part of analysis variables, the cloudy radiance observation operator via Community Radiative Transfer Model (CRTM; John-

Satellite	Sensor	Clear-sky channels (Frequency, GHz)	All-sky channels (Frequency, GHz)
Aqua	AMSU-A	8 (55.5), 9 (57.290344)	-
NOAA-15	AMSU-A	5 (53.596 ± 0.115), 7 (54.94), 8 (55.5), 9 (57.290344)	$1 (23.8), 3 (31.4), 4 (52.8), 15 (89 \pm 1.00)$
NOAA-18	AMSU-A	5 (53.596 ± 0.115), 6 (54.4), 7 (54.94), 8 (55.5), 9 (57.290344)	$1 (23.8), 3 (31.4), 4 (52.8), 15 (89 \pm 1.00)$
	MHS	$3 (183.311 \pm 1.00), 4 (183.311 \pm 3.00), 5 (190.311)$	_
NOAA-19	AMSU-A	$5 (53.596 \pm 0.115), 6 (54.4), 7 (54.94), 9 (57.290344)$	$1 (23.8), 3 (31.4), 4 (52.8), 15 (89 \pm 1.00)$
	MHS	$3 (183.311 \pm 1.00), 4 (183.311 \pm 3.00), 5 (190.311)$	_
Metop-A	AMSU-A	5 (53.596 ± 0.115), 6 (54.4), 9 (57.290344)	$1 (23.8), 3 (31.4), 4 (52.8), 15 (89 \pm 1.00)$
	MHS	$3 (183.311 \pm 1.00), 4 (183.311 \pm 3.00), 5 (190.311)$	_
Metop-B	AMSU-A	8 (55.5), 9 (57.290344)	$1 (23.8), 3 (31.4), 4 (52.8), 15 (89 \pm 1.00)$
	MHS	$3 (183.311 \pm 1.00), 4 (183.311 \pm 3.00), 5 (190.311)$	-

Table 2. AMSU-A and MHS channels (frequency, GHz) assimilated using clear-sky or all-sky approach.

son et al., 2023), and situation-dependent all-sky observation error models (Geer and Bauer, 2011). Since the WSM6 microphysics scheme is employed, the mixing ratios of Q_c , Q_i , Q_r , Q_s , and Q_g are used as the hydrometeor analysis variables. For the window channels assimilated using the all-sky approach, only over-water radiances are assimilated due to the large uncertainty of surface emissivity over the land, snow, and ice surfaces. As in Liu et al. (2022), the all-sky observation error for each AMSU-A window channel is modelled as a piecewise linear ramp function of the average of cloud liquid water (CLW) path retrieved from the observed and CRTM-simulated (from the background) radiances of AMSU-A channels 1 and 2. For each channel, two CLW thresholds are defined. Observations with an averaged CLW below the lower threshold are treated as clear-sky and assigned the clear-sky observation error, while those above the upper threshold use the all-sky observation error. For averaged CLW values between the thresholds, the observation error increases linearly from the clear-sky to the all-sky observation error as the averaged CLW increases. This approach makes the all-sky observation error cloud-dependent, accounting for cloud-related uncertainties arising from both the observations and the background. More details about the all-sky observation error model are given by Liu et al. (2022).

3.3 Experimental design

Six 6-hourly cycled 80-member ensemble analysis and forecasting experiments are conducted as summarized in Table 3. Experiment AllSky serves to evaluate the impact of allsky radiance DA compared to ClrSky, the clear-sky radiance DA experiment. The other four experiments explore different settings for covariance inflation and localization, and motivate the specific combination of the inflation and localization used in ClrSky and AllSky. All experiments begin from a time-lagged ensemble background valid at 00:00 UTC on 15 April 2018. The time-lagged ensemble background is generated using four sets of 20-member ensemble forecasts of different lead times (24, 18, 12, and 6 h), initialized from Global Ensemble Forecast System (GEFS) ensemble analyses valid at 00:00, 06:00, 12:00, and 18:00 UTC on 14 April 2018, respectively. The assimilation period for the experiments ClrSky and All-Sky is nearly one month, with the last analysis cycle being 12:00 UTC on 14 May 2018, while the other experiments span the first 10 d of that period.

In ClrSky, the non-radiance observations and clear-sky radiances from AMSU-A temperature sounder channels and MHS water vapor channels are assimilated (see Table 2). For the rest of the experiments, radiances from AMSU-A window channels under all-weather situations are assimilated in addition to those assimilated in ClrSky.

The AllSky-RTPS, AllSky-RTPP, and AllSky are conducted to evaluate the sensitivity to the covariance inflation with the same setting for the covariance localization. Following Guerrette et al. (2023), the RTPS is employed in AllSky-RTPS with $\alpha_{RTPS} = 1.0$, and RTPP is used in AllSky-RTPP with $\alpha_{RTPP} = 0.7$. Following Met Office's EDA system (Bowler et al., 2017), RTPP and RTPS are applied sequentially in AllSky, with $\alpha_{RTPP} = 0.5$ and $\alpha_{RTPS} = 0.9$. The AllSky, AllSky-L1200, and AllSky-L600 use the same setting for the inflation but use horizontal localization scales of 300, 1200, and 600 km, respectively, for all-sky AMSU-A channels. In all experiments, the horizontal localization scale is set to 1200 km for the non-radiance data and clear-sky AMSU-A and MHS radiances, following Liu et al. (2022) and Guerrette et al. (2023), while the vertical localization scale is set to 6 km.

Experiments Inflation Horizontal localization scale (km) Clear-sky channel All-sky channel ClrSky $\alpha_{\text{RTPS}} = 0.9, \alpha_{\text{RTPP}} = 0.5$ 1200 AllSky $\alpha_{\text{RTPS}} = 0.9, \alpha_{\text{RTPP}} = 0.5$ 1200 300 AllSky-RTPS $\alpha_{\text{RTPS}} = 1.0$ 1200 300 AllSky-RTPP $\alpha_{\text{RTPP}} = 0.7$ 1200 300 AllSky-L1200 1200 $\alpha_{\text{RTPS}} = 0.9, \alpha_{\text{RTPP}} = 0.5$ 1200 AllSky-L600 $\alpha_{\text{RTPS}} = 0.9, \alpha_{\text{RTPP}} = 0.5$ 1200 600

Table 3. Inflation and horizontal localization configurations for six experiments.

4 Results from inflation and localization sensitivity experiments

Due to the limited ensemble size, the EnKF-based methods suffer from sampling errors, which can lead to filter divergence and degraded analysis. To combat the sampling errors, the covariance inflation and localization techniques are commonly employed in the EnKF-based methods. In this section, we provide the results for the sensitivity to the covariance inflation setting first and then for the sensitivity to the horizontal localization setting for all-sky AMSU-A radiances.

4.1 Sensitivity to covariance inflation configuration

Many studies have emphasized the sensitivity of analysis performance to the choice of inflation parameters (e.g., Whitaker and Hamill, 2012; Nerger, 2015). Kotsuki et al. (2017) found that using either RTPP or RTPS alone could lead to an over-dispersive ensemble in certain regions, and that this behavior could be resolved by using a combination of additive and multiplicative inflations. Bowler et al. (2017) found that a combination of RTPS and RTPP could maintain ensemble spread and reduce forecast errors in the Met Office's EDA system. Given that the additive inflation is not implemented yet in the current JEDI system, we only examine the multiplicative inflation techniques with RTPP or RTPS alone in AllSky-RTPP and AllSky-RTPS, or with a combination of RTPP and RTPS in AllSky.

Figure 2 shows the time series of the model-space ensemble spread and ensemble-mean root-mean-square error (RMSE) of the background 6 h forecast for the vertically-averaged U, V, T, and water vapor mixing ratio (Q_v) fields of the three experiments, with the GFS analyses treated as the truth. Due to the temperature bias near the model top (Liu et al., 2022), the evaluation of T is limited to below model level 50 (\sim 25 km a.g.l.). Both AllSky-RTPP and AllSky-RTPS, applying RTPP or RTPS alone, present a consistent trend that the ensemble spread (solid black and blue curves) gradually decreases with assimilation cycles for all the four variables. Consequently, the ensemble-mean RMSE gradually increases over time. In contrast, the ensemble spread in All-Sky with a combination of RTPP and RTPS is the largest and

well maintained over time, with the corresponding ensemblemean RMSE being the smallest among the three experiments. This result is consistent with Bowler et al. (2017) using an EDA system.

The benefits of employing a combination of RTPP and RTPS are also evident when verified against observations. Figure 3 shows the vertical profiles of the observation-space total spread (i.e., square root of the sum of the ensemble variance and observation error variance) and ensemble-mean RMSE of the background, verified against radiosonde observations. For a good ensemble DA system, the total spread is expected to be comparable with the ensemble-mean RMSE. AllSky outperforms AllSky-RTPP and AllSky-RTPS by producing the largest total spread and the smallest ensemblemean RMSEs in all observed variables at almost all levels. However, the total spread smaller than the ensemble-mean RMSE for certain levels of U, V, and T also suggests that further improvement is needed by tuning observation errors and/or inflation/localization settings in a future study. This issue has also been observed in MPAS-JEDI's EDA system (Guerrette et al., 2023).

It is worth mentioning that the model errors are not taken into account due to the lack of stochastics physics parameterization schemes (Buizza et al., 1999; Berner et al., 2009) in the current MPAS-A model. It is anticipated that the ensemble DA performance with MPAS-JEDI could be improved by introducing stochastics physics or using a multi-physics approach in the ensemble forecast step. In addition, optimal inflation configurations may depend on factors such as ensemble size, mesh resolution, and other DA settings. Developing robust and generally applicable inflation strategies therefore requires further systematic investigation.

4.2 Sensitivity to horizontal localization scale for all-sky radiances

In the global EnKF-based systems, it is a common practice to use a relatively large horizontal localization scale for satellite radiances (e.g., 1200 km in Lei et al., 2020 and 1000 km in Bonavita et al., 2020). Previous studies also show the benefits of using a shorter horizontal localization scale for all-sky satellite radiances in the regional EnKF-

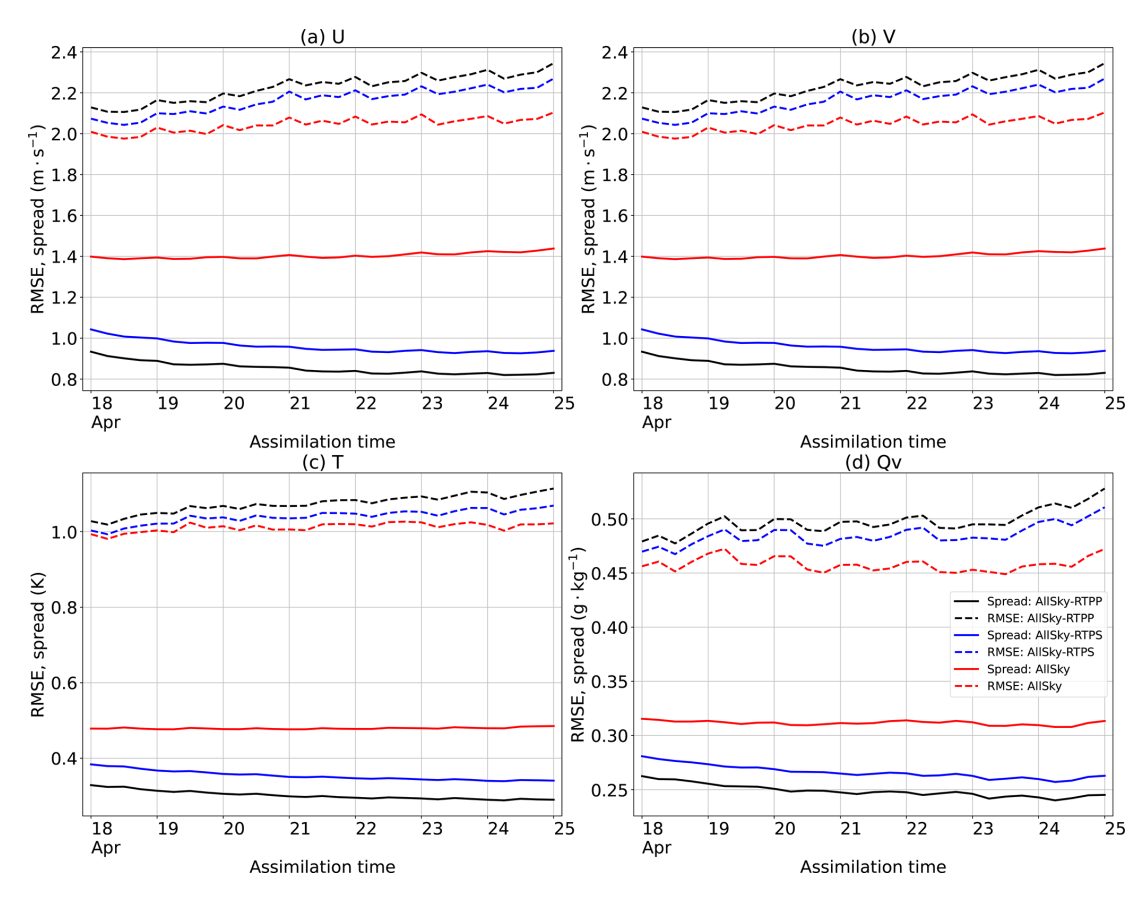


Figure 2. Time series of the model-space ensemble spread (solid lines) and ensemble-mean RMSE (dashed lines) of the background 6 h forecast verified against the GFS analyses for the vertically-averaged (a) U, (b) V, (c) T, and (d) Q_V fields from the three experiments. Statistics are calculated globally below model level 50 between 00:00 UTC 18 April and 00:00 UTC 25 April 2018 at an interval of 6 h.

based systems. Okamoto et al. (2019) found that using a horizontal localization scale of 365 km for Himawari-8 radiance assimilation improved the fit of the background to radiosonde observations compared to using a horizontal localization scale of 730 km in their regional LETKF system. Bonavita et al. (2020) also showed that reducing the horizontal localization scale for all-sky satellite radiances from 2000 to 1000 km produced $\sim 1\,\%$ improvement in ECMWF's global EnKF system. Therefore, we further evaluate the sensitivity of horizontal localization scales for AMSU-A window channel all-sky radiances by comparing AllSky-L1200, AllSky-L600, and AllSky.

Figure 4 illustrates the percentage difference in the ensemble-mean RMSE of U, V, T, and $Q_{\rm v}$, verified against the GFS analyses, for AllSky-L600 and AllSky relative to AllSky-L1200, at different model level and latitude bins. Following Guerrette et al. (2023), the bootstrap resampling method is employed to calculate the confidence intervals of the differences. The samples are resampled 10 000 times with replacement, and the 95 % confidence intervals are obtained using the percentile method (Gilleland et al., 2018), corresponding to the 2.5th and 97.5th percentiles of the boot-

strap distribution. It can be clearly seen that using a 600 km localization scale in AllSky-L600 reduced RMSEs for all the four variables at most latitude bins and model levels, with a larger improvement over the southern hemisphere, when compared to AllSky-L1200 with a 1200 km localization scale. Decreasing the localization scale to 300 km in All-Sky further improved the short-term forecasts as indicated by model/latitude bins with darker blue colour in the right column of Fig. 4. Given the overall superior performance of using 300 km localization scale, and considering that 300 km is sufficiently small relative to the model mesh resolution of 60 km, we did not further test shorter horizontal localization scales, even though they might offer further improvements. Consequently, the AllSky experiment was extended to cover the full month and is compared with the ClrSky experiment in the next section.

5 Impact of all-sky radiance DA

This section evaluates the impact of all-sky AMSU-A radiance DA for the short-term background forecasts (i.e., 6h

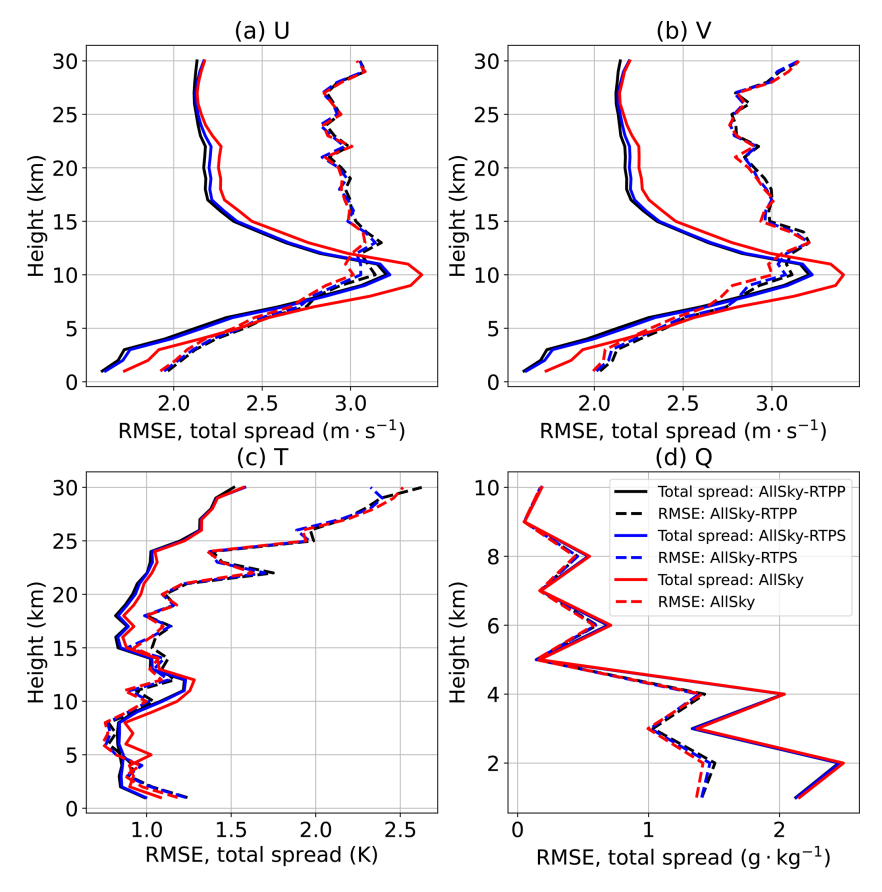


Figure 3. Vertical profiles of the observation-space ensemble total spread (solid lines) and ensemble-mean RMSE (dashed lines) of the background verified against radiosonde (a) U, (b) V, (c) T, and (d) Q observations. Statistics are calculated globally from the ensemble background between $00:00\,\mathrm{UTC}$ 18 April and $00:00\,\mathrm{UTC}$ 25 April 2018 at an interval of 12 h.

lead time) first and then for the extended-range forecasts up to 7 d.

5.1 6 h forecasts

Figure 5 shows the percent RMSE difference of the ensemble mean of 6 h forecasts for U, V, T, and $Q_{\rm v}$ of AllSky relative to ClrSky, when verified against the GFS analyses. Positive impacts (model level/latitude bins with blue colour) occur for U, V, and $Q_{\rm v}$ almost everywhere between 50° S and 50° N, with largest improvements in the tropics. There are some degradations for these three variables at the high latitudes and below the model level 30 (for U and V) or 20 (for $Q_{\rm v}$) over the southern hemisphere. Largest degradation is seen in T in the latitude band of 50–60° S and between model levels 5 and 15.

Additional evidence of temperature degradation associated with all-sky radiance assimilation is observed when verified against clear-sky radiances. Figure 6 shows the latitude-binned RMS and mean of ensemble mean background minus observations for bias-corrected clear-sky radiances from five AMSU-A temperature sounding channels aboard NOAA 18. Assimilation of AMSU-A window channels produces more

noticeable differences between ClrSky and AllSky in channels 5, 6, and 7, which are sensitive to lower and middle atmospheric levels where clouds and precipitation are prevalent. As expected, AllSky reduces the mean value statistics in these channels because the inclusion of more cloud-affected observations reduces the simulated brightness temperatures. Notably, at lower latitudes, AllSky yields slightly smaller RMS values and mean OMB values closer to zero, indicating benefits of all-sky assimilation. However, between 50 and 70° S, AllSky exhibits a more pronounced cold bias than ClrSky in channel 5, accompanied by a marked RMS increase, consistent with the temperature degradation highlighted in Fig. 5. In contrast, channels 8 and 9, which are less sensitive to cloud-affected layers, show only minor differences between both experiments.

The temperature degradation in the southern midlatitudes aligns with challenges documented in other systems. A similar pattern was reported in the ECMWF's 4DVar system when assimilating all-sky AMSU-A channel 4 radiances (Weston et al., 2019). Lonitz and Geer (2015) attributed such issue to model deficiencies in representing liquid water in cold-sector clouds over the Southern oceans – a microphys-

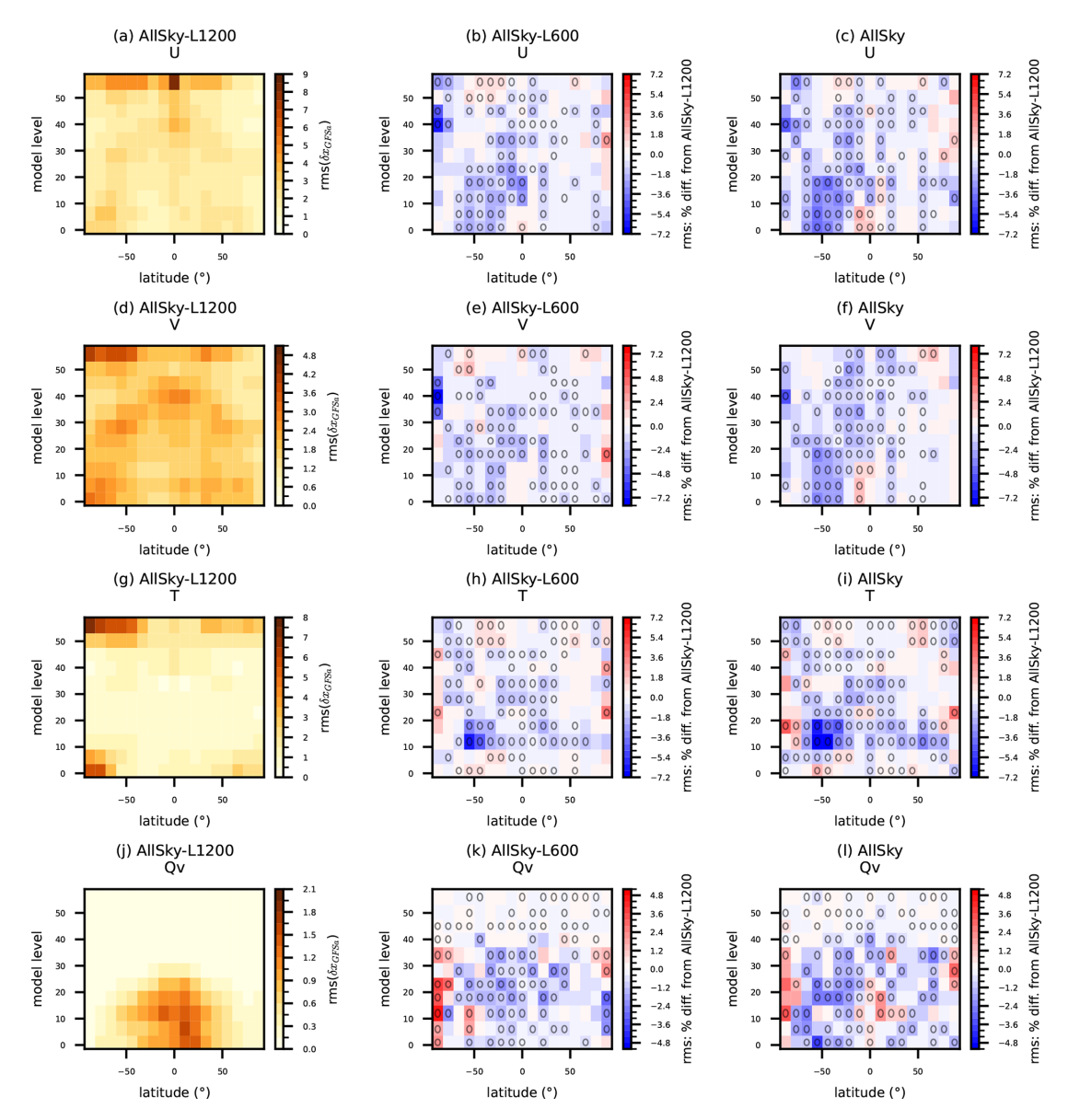


Figure 4. Left: RMSE of AllSky-L1200's ensemble mean background for U, V, T, and Q_v ; Middle/Right: percent difference in RMSE for AllSky-L600 and AllSky, relative to AllSky-L1200. The RMSEs are computed using the GFS analyses as the reference and the statistics are binned with 5 model levels and 11° latitude bands. Inset black circles in individual bins indicate that the difference in RMSE between experiments is statistically significant with a 95% confidence interval, as determined via bootstrap resampling from 29 samples spanning 00:00 UTC 18 April to 00:00 UTC 25 April 2018 at 6 h intervals.

ical bias likely presents in other forecast systems as well (Tong et al., 2020). Given these similarities, we suspect that MPAS also suffers from similar microphysical bias. To address this, a screening procedure for such cold-sector clouds, following Lonitz and Geer (2015), could be developed for MPAS-JEDI. Note that the current bias correction scheme for all-sky radiances is still based upon the existing clear-sky approach and updated by an independent cycling deterministic DA system, which is sub-optimal. We plan to introduce cloud-/precipitation-related predictors for the bias correction of all-sky radiance DA, which has been shown to improve

all-sky infrared radiance DA (Okamoto et al., 2023). Implementation of an online bias correction method, where correction coefficients are included as part of the analysis variables (Fertig et al., 2009; Miyoshi et al., 2010; Chandramouli et al., 2022), is also under consideration for MPAS-JEDI's LGETKF.

5.2 7 d forecasts

We initialized 7 d forecasts from the ensemble mean analysis at 00:00 UTC each day from 18 April to 14 May 2018, for

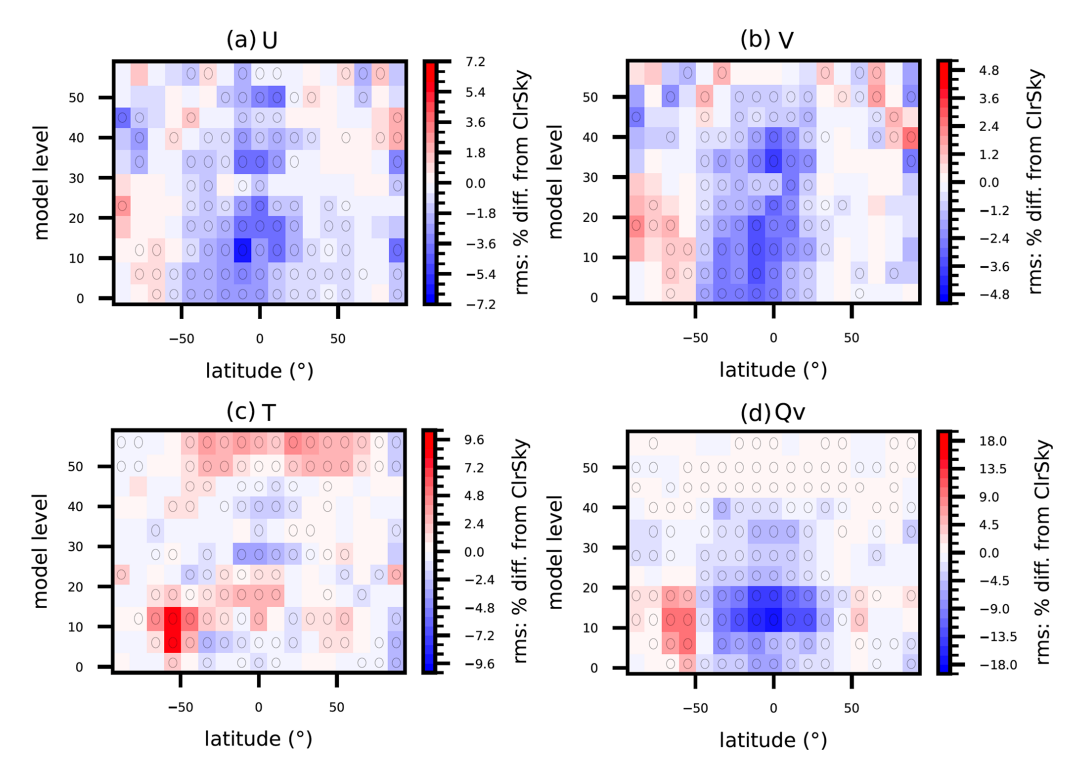


Figure 5. Percent difference in RMSE for AllSky relative to ClrSky for (a) U, (b) V, (c) T, and (d) Q_V of the ensemble mean of 6 h forecasts. Inset black circles in individual bins indicate that the difference in RMSE between experiments is significant with a 95 % confidence interval, as determined via bootstrap resampling from 104 samples spanning 00:00 UTC 18 April to 18:00 UTC 14 May 2018 at 6 h intervals.

a total of 27 forecasts. The first three days (15–17 April) are treated as a spin-up period for the DA cycles to reach MPAS-JEDI's own cycling climatology and are excluded from the extended forecast evaluation.

5.2.1 Model space verification

The relative RMSE differences of AllSky from ClrSky as a function of forecast lead time, when verified against GFS analyses for the vertically-averaged upper-air fields over different regions, are shown in Fig. 7. The largest percent improvement from AllSky occurs for Q_v with a 3 %–6 % RMSE reduction for the day-1 forecast over the tropical regions. The statistically significant improvement for $Q_{\rm v}$ lasts up to 7 d over the ITCZ and 5-6 d over northern and southern tropical regions. A smaller positive impact of AllSky on $Q_{\rm v}$ lasts up to 3 d over the southern extratropic region with a mostly neutral impact over the northern extratropic. Similar positive impact of AllSky can also be seen for the Uand V-wind components with the statistically significant improvement lasting up to 7 d for the U-wind component, but only up to 5 d for the V-wind component over the ITCZ and northern tropical regions. Consistent with some short-term forecast degradation in T (Fig. 5c) in AllSky, the negative impact is also seen for the first 2-3 d, and then the impact becomes neutral and even positive over some regions, although not statistically significant.

Figure 8 shows the relative RMSE differences between ClrSky and AllSky for surface variables verified against GFS analyses. Consistent with the impact on the upper air variables in Fig. 7, the largest and most significant positive impact from AllSky is on 2 m Q_v with a \sim 2.8 % RMSE reduction for the day-1 forecasts and a $\sim\!0.5\,\%$ RMSE reduction still remaining for the day-6 forecasts. The positive impact of AllSky on the 10 m U-wind component is also evident with a smaller variation of the percent RMSE reduction ($\sim 0.5 \%$) ~ 1 %) for the first five days, but less significant than the impact on $Q_{\rm v}$. Similar to the upper-air T forecasts, the all-sky DA also slightly degrades the 2 m T forecasts for the first 4 d and then improves forecasts from day-5. For the surface pressure forecasts, the AllSky experiment mostly outperforms the ClrSky experiment for all the forecast ranges, except for the first day forecast, with a maximum improvement of 2 % at day-5.

These model-space verification results for AllSky vs. ClrSky are overall consistent with those of Liu et al. (2022), who evaluated the impact of all-sky AMSU-A radiance DA above the clear-sky AMSU-A radiances using MPAS-JEDI's 3DEnVar. This study with MPAS-JEDI's LGETKF evaluates the impact of all-sky AMSU-A radiance DA above clear-sky radiances from both AMSU-A and MHS, i.e., a more challenging impact assessment with more clear-sky radiance data

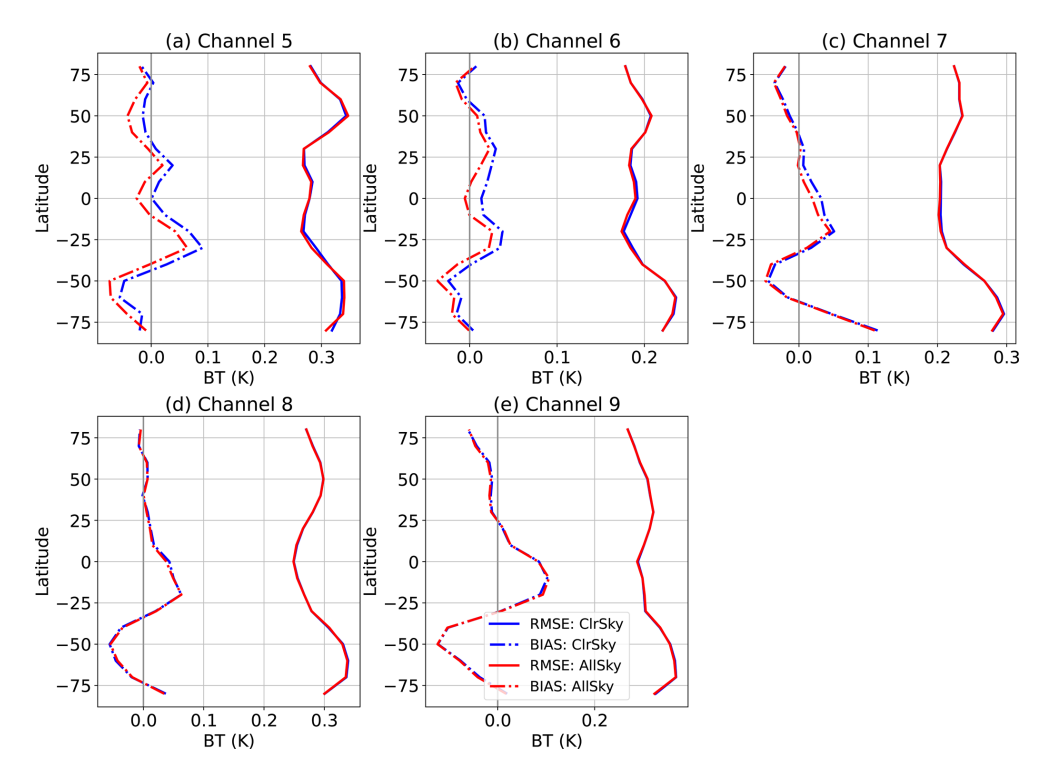


Figure 6. RMS (solid line) and mean (dashed line) of the ensemble mean background minus observations, binned by latitude, for bias-corrected clear-sky radiances from NOAA 18 AMSU-A: (a) channel 5, (b) channel 6, (c) channel 7, (d) channel 8, and (e) channel 9, for ClrSky (blue) and AllSky (red). Statistics are calculated globally every 6 h from 00:00 UTC 18 April to 12:00 UTC 14 May 2018, using 10° latitude bins.

in the benchmark experiment, leading to a smaller magnitude of improvement than that of Liu et al. (2022).

5.2.2 Observation space verification

The forecast impacts of all-sky DA are further evaluated with radiosonde observations and independent (i.e., not assimilated) Advanced Technology Microwave Sounder (ATMS) radiances in all-weather situations. Similar to the upper-air model-space verification, all-sky AMSU-A radiance DA improves the forecasts of U, V, and Q, but degrades the forecasts of T, when verified against the radiosonde observations (Fig. 9). While all-sky AMSU-A radiances are assimilated only over water, radiosonde data are mostly available over land. It could take several days for the positive impacts to propagate from the seas to the land areas, likely leading to the positive impact being the largest in the day-5 or day-6 for the forecasts of U, V, and Q, compared to the largest positive impacts observed in the first day in the global average in Fig. 7.

Figure 10 shows the relative forecast RMSE differences between AllSky and ClrSky, when verified against brightness temperatures of nine ATMS channels from NOAA-20. The nine ATMS channels include three window channels (1, 2, and 3) sensitive to cloud and precipitation, three temperature sounding channels (5, 7, and 9), and three water vapor

channels (18, 19, and 20). The MPAS-JEDI's HofX application is employed to calculate the simulated brightness temperatures using the cloudy CRTM operator with the day-1 to day-7 forecasts as input. The verification statistics are calculated only over water for the three window channels and over both water and land for the other six channels. The benefit of assimilating all-sky AMSU-A radiances is larger on clouds than on moisture as evidenced with a larger RMSE reduction for the three window channels than for the three water vapor channels. Interestingly, the positive impact of AllSky is found for the three temperature channels throughout the 7 d forecasts, unlike the negative T impact in model space verification for the first 3 d forecasts in Fig. 7c. This discrepancy should be caused by the model-space T verification being vertically and globally averaged and the three ATMS temperature channels sensing different layers of the atmosphere, with the channel 5 for a layer around 850 hPa, the channel 7 around 400 hPa, and the channel 9 around 200 hPa.

6 Conclusions

In this study, the LGETKF algorithm within the JEDI framework is implemented in MPAS-JEDI along with the capability of assimilating clear-sky and all-sky satellite radiance data. As the first implementation and evaluation of MPAS-

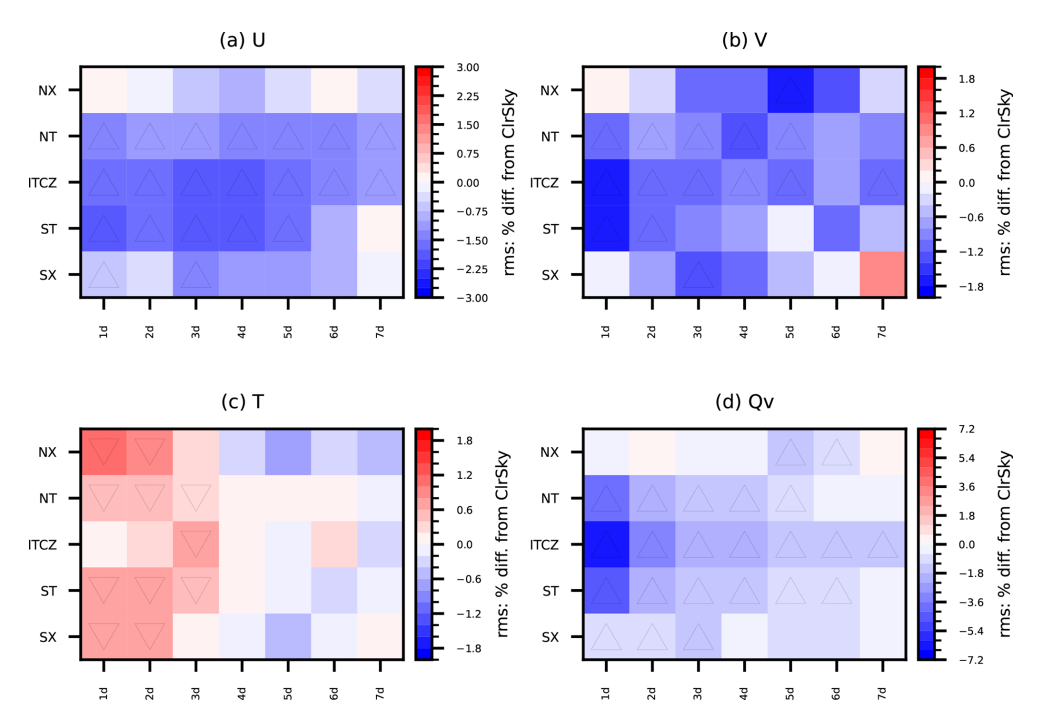


Figure 7. The differences in RMSE of the upper-air (a) U, (b) V, (c) T, and (d) Q_V between ClrSky and AllSky as a function of forecast lead time and regions, using GFS analyses as reference. Regions are defined as NX (northern extratropic; 30–90° N), NT (northern tropical; 5–30° N), ITCZ (intertropical convergence zone; 5° S–5° N), ST (southern tropical; 5–30° S), and SX (southern extratropic; 30–90° S). The upward (downward) black triangles indicate the statistically significant improvements (degradations) at the 95 % confidence level, as determined via bootstrap resampling from 27 daily samples spanning 18 April to 14 May 2018.

JEDI's LGETKF, this study investigates its computational behaviour, optimal configuration, and performance through a series of sensitivity experiments and 1-month cycled DA experiments, demonstrating the stable and robust performance of MPAS-JEDI's LGETKF for community research and potential operational applications.

The LGETKF performs vertical localization in model space, making it suitable for assimilating nonlocal observations such as satellite radiances, but with additional cost for the computation of HofXs related to the modulated ensemble members. Performing the Observer and Solver steps separately with different jobs allows the use of different parallelization strategies for the observation distribution across processing elements, which improves the computational efficiency of MPAS-JEDI's LGETKF. Additionally, computing the HofX of each ensemble member in parallel further reduces the overall time required to complete the LGETKF analysis.

The impacts of assimilating over-water all-sky radiances from AMSU-A window channels are investigated with a global 80-member LGETKF at a quasi-uniform grid spacing of 60 km over a one-month period. The efforts are made to tune the covariance inflation and horizontal localization first. Results indicate that combining RTPS and RTPP for the inflation is more effective than using RTPS or RTPP alone in maintaining the ensemble spread over time and per-

forms the best with the smallest RMSE of the ensemble mean background. The sensitivity experiments also demonstrate the benefits of using a smaller horizontal localization scale for all-sky AMSU-A radiances. The model-space verification shows the overall positive impacts of all-sky AMSU-A radiance DA, when compared to the benchmark experiment assimilating clear-sky AMSU-A and MHS radiances, on the forecasts of moisture and wind fields with the largest improvement over the tropical regions up to 7 d. All-sky AMSU-A DA also leads to an improved forecast fitting to the ATMS window channels' radiances, indicating a better forecast of clouds and precipitation. All-sky AMSU-A DA impact from this study is mostly consistent with Liu et al. (2022) using MPAS-JEDI's 3DEnVar.

One issue from all-sky AMSU-A DA, which was also seen from previous studies, is the degradations of temperature forecast, especially at the lower troposphere around 60° S where the forecasts are likely biased due to the model deficiency in simulating cold-air outbreaks. This issue could be resolved by applying more strict quality control, improving physical parameterization of the model, enhancing radiance bias correction scheme, or revisiting the all-sky observation error model. Despite the efforts for tuning the inflation and the localization configurations, the ensemble of LGETKF is still sub-optimal with insufficient ensemble spreads, especially in the upper troposphere and stratosphere.

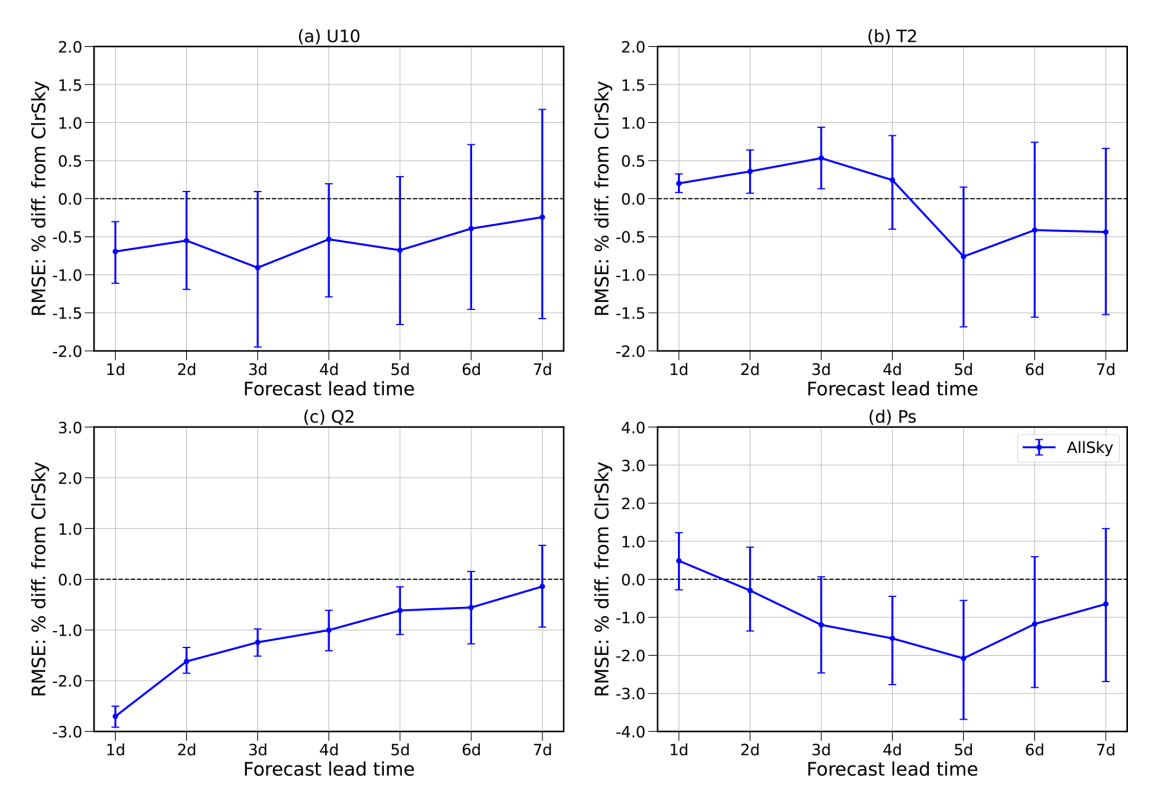


Figure 8. Similar to Fig. 7, but for the global statistics of percent RMSE differences for (a) 10 m U (U_{10}), (b) 2 m T (T_2), (c) 2 m Q_V (Q_2), and (d) surface pressure (P_s). The bars below or above zero indicate that the difference is statistically significant at a 95 % confidence interval, as determined via bootstrap resampling from 27 daily samples spanning 18 April to 14 May 2018.

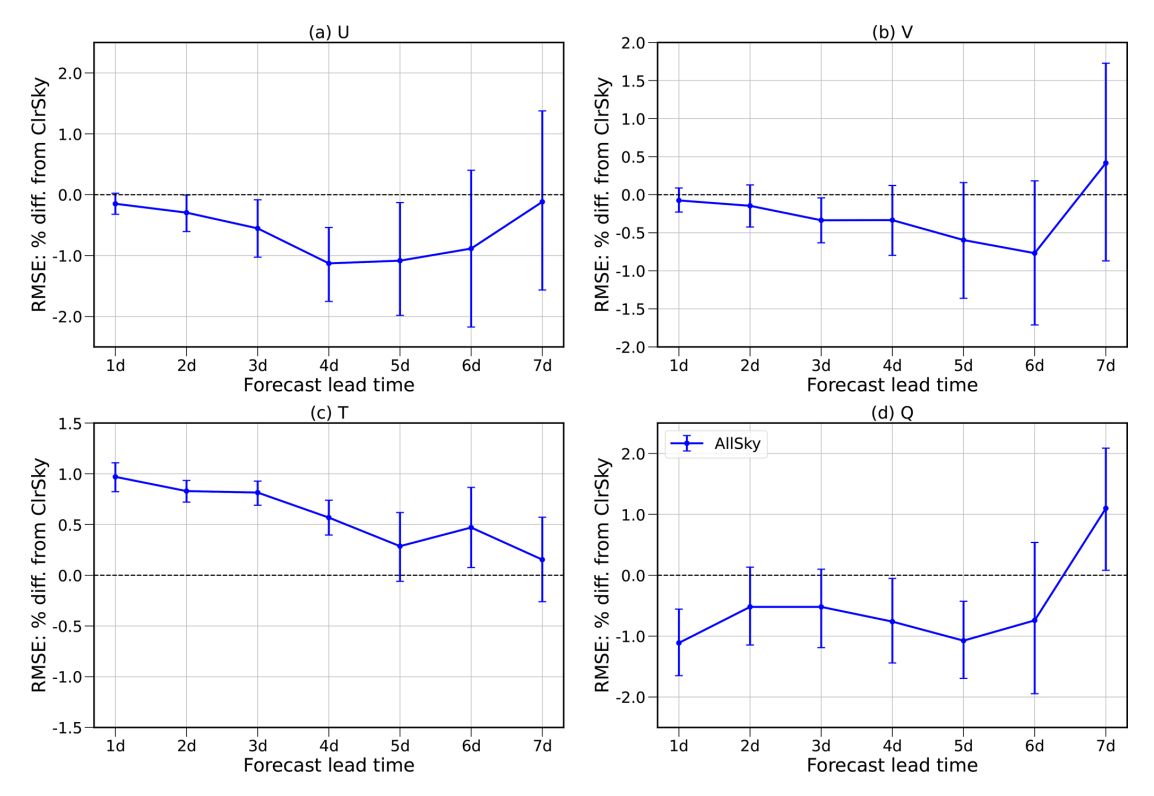


Figure 9. Similar to Fig. 8, but verified the forecasts against radiosonde (a) U, (b) V, (c) T, and (d) Q observations.

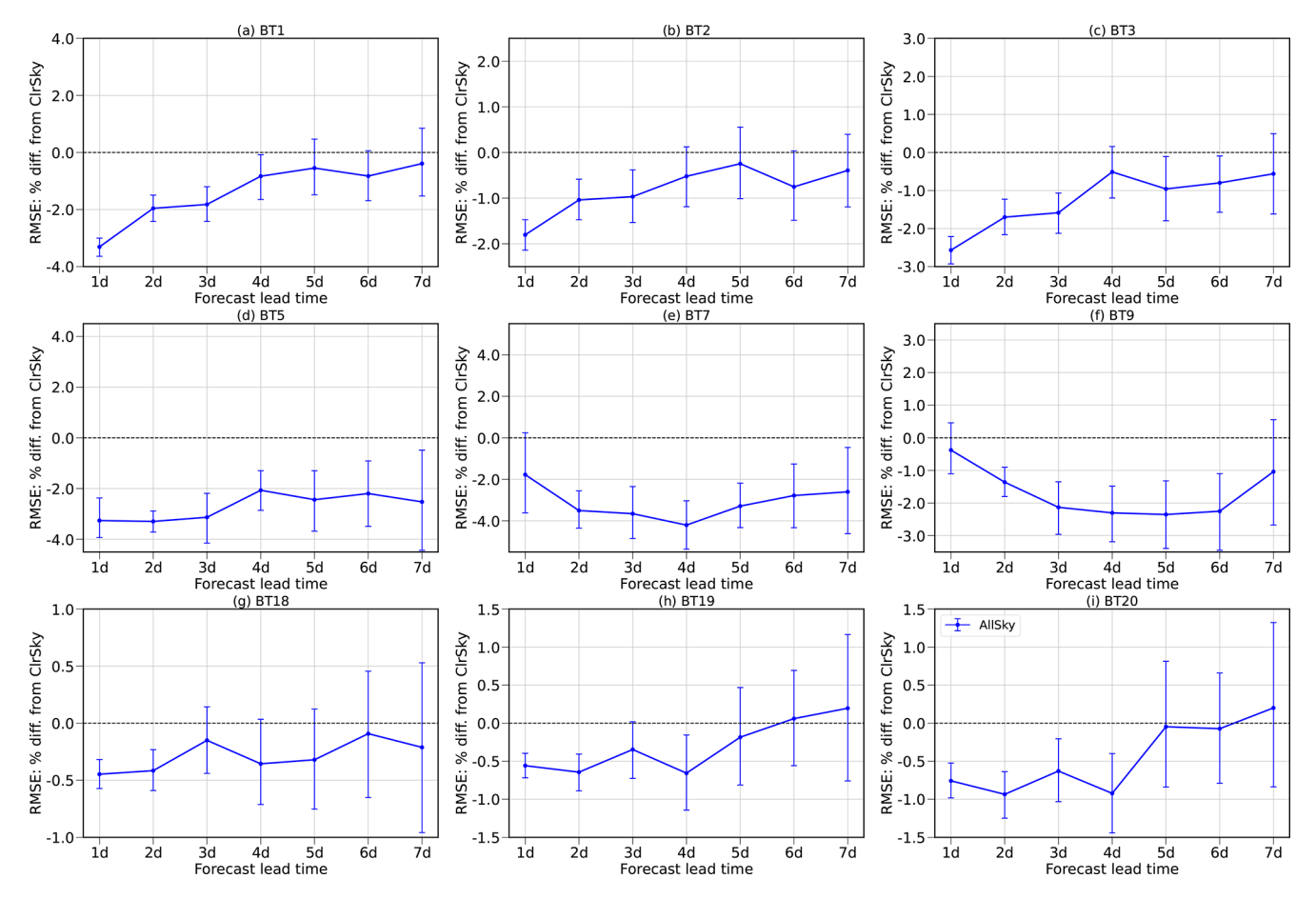


Figure 10. Similar to Fig. 9, but verified the forecasts against brightness temperatures of nine ATMS channels from NOAA-20.

Further improvements could be made with spatially and temporally adaptive inflation factors (Anderson, 2009) or scale-dependent localization (Wang et al., 2021). A better specification of the observation errors using the statistical method of Desroziers et al. (2005) will also improve the analysis accuracy in general. Also, an ensemble-based forecast sensitivity to observations (EFSO; Liu and Kalnay, 2008; Kalnay et al., 2012) diagnosis tool has been developed for MPAS-JEDI's LGETKF to estimate the impacts of assimilated observations on short-term forecasts. This tool could be used to further investigate the effects of all-sky assimilation and to enhance the performance of MPAS-JEDI's LGETKF.

MPAS-JEDI's LGETKF has the capability to assimilate all-sky radiance data from a wide range of microwave and infrared sensors, and we plan to explore them in future studies. The regional DA capability of MPAS-JEDI is under active development, and the application of the EnKF-based methods to convective-scale DA is already underway.

Author contributions. TS designed, conducted, and analysed all experiments and wrote the manuscript. JJG initialized the LGETKF implementation in MPAS-JEDI. JB configured the all-sky assimi-

lation of AMSU-A radiances. ZL and CS aided with experimental design and analysis. All co-authors contributed to the development of the MPAS-JEDI, preparation of externally sourced data, design of experiments, and preparation of the manuscript.

Code and data availability. The source code of MPAS-JEDI 2.1.0 is available on Zenodo at https://doi.org/10.5281/zenodo.15201032 (Joint Center for Satellite Data Assimilation and National Center for Atmospheric Research, 2023). Global Forecast System analyses are available from NCAR Research Data Archive (RDA) https://gdex.ucar.edu/datasets/d084001/ (last access: 17 October 2025; National Centers for Environmental Prediction/National Weather Service/NOAA/U.S. Department of Commerce, 2015). Global Ensemble Forecast System ensemble analyses are downloaded from https://www.ncei.noaa.gov/products/ weather-climate-models/global-ensemble-forecast (last access: 17 October 2025; NOAA, 2025). Conventional and satellite observations assimilated are downloaded from NCAR RDA https:// rda.ucar.edu/datasets/d337000 (last access: 17 October 2025; National Centers for Environmental Prediction/National Weather Service/NOAA/U.S. Department of Commerce, 2008) and https:// rda.ucar.edu/datasets/d735000/ (last access: 17 October 2025; National Centers for Environmental Prediction/National Weather Service/NOAA/U.S. Department Of Commerce, 2009). ATMS radiance data used in the forecast verification are downloaded from https://sounder.gesdisc.eosdis.nasa.gov/opendap (last access: 17 October 2025; NASA, 2025).

Competing interests. The contact author has declared that none of the authors has any competing interests.

Disclaimer. Publisher's note: Copernicus Publications remains neutral with regard to jurisdictional claims made in the text, published maps, institutional affiliations, or any other geographical representation in this paper. While Copernicus Publications makes every effort to include appropriate place names, the final responsibility lies with the authors. Views expressed in the text are those of the authors and do not necessarily reflect the views of the publisher.

Acknowledgements. The National Center for Atmospheric Research (NCAR) is sponsored by the National Science Foundation of the United States. The numerical calculations of this study are supported by NCAR's Computational and Information Systems Laboratory (CISL). We thank Sergey Frolov, Wei Huang, and Bo Huang in NOAA Physical Sciences Laboratory for valuable discussions.

Financial support. This research has been supported by the United States Air Force (grant no. NA21OAR4310383).

Review statement. This paper was edited by Guoqing Ge and reviewed by two anonymous referees.

References

- Anderson, J., Hoar, T., Raeder, K., Liu, H., Collins, N., Torn, R., and Avellano, A.: The Data Assimilation Research Testbed: A Community Facility, Bull. Amer. Meteor. Soc., 90, 1283–1296, https://doi.org/10.1175/2009BAMS2618.1, 2009.
- Anderson, J. L.: Spatially and temporally varying adaptive covariance inflation for ensemble filters, Tellus A, 61, 72–83, https://doi.org/10.1111/j.1600-0870.2008.00361.x, 2009.
- Anderson, J. L.: An Ensemble Adjustment Kalman Filter for Data Assimilation, Mon. Weather Rev., 129, 2884–2903, https://doi.org/10.1175/1520-0493(2001)129<2884:AEAKFF>2.0.CO;2, 2001.
- Bauer, P., Geer, A. J., Lopez, P., and Salmond, D.: Direct 4D-Var assimilation of all-sky radiances, Quart. J. Roy. Meteor. Soc., 136, 1868–1885, https://doi.org/10.1002/qj.659, 2010.
- Berner, J., Shutts, G. J., Leutbecher M., and Palmer, T. N.: A spectral stochastic kinetic energy backscatter scheme and its impact on flow-dependent predictability in the ECMWF ensemble prediction system, J. Atmos. Sci., 66, 603–626, https://doi.org/10.1175/2008JAS2677.1, 2009.
- Bishop, C. H., Whitaker, J. S., and Lei, L.: Gain Form of the Ensemble Transform Kalman Filter and Its Relevance to Satellite Data Assimilation with Model Space Ensemble Co-

- variance Localization, Mon. Weather Rev., 145, 4575–4592, https://doi.org/10.1175/MWR-D-17-0102.1, 2017.
- Bonavita, M., Geer, A. J., and Hamrud, M.: All-Sky Microwave Radiances Assimilated with an Ensemble Kalman Filter, Mon. Weather Rev., 148, 2737–2760, https://doi.org/10.1175/MWR-D-19-0413.1, 2020.
- Bowler, N. E., Clayton, A. M., Jardak, M., Lee, E., Lorenc, A. C., Piccolo, C., Pring, S. R., Wlasak, M. A., Barker, D. M., Inverarity, G. W., and Swinbank, R.: Inflation and localization tests in the development of an ensemble of 4D-ensemble variational assimilations, Q. J. R. Meteorol. Soc., 143, 1280–1302, https://doi.org/10.1002/qj.3004, 2017.
- Buizza, R., Miller, M., and Palmer, T. N.: Stochastic representation of model uncertainties in the ECMWF ensemble prediction system, Q. J. Roy. Meteor. Soc., 125, 2887–2908, https://doi.org/10.1002/qj.49712556006, 1999.
- Campbell, W. F., Bishop, C. H., and Hodyss, D.: Vertical covariance localization for satellite radiances in ensemble Kalman filters, Mon. Weather Rev., 138, 282–290, https://doi.org/10.1175/2009MWR3017.1, 2010.
- Chan, M.-Y., Zhang, F., Chen, X., and Leung, L. R.: Potential impacts of assimilating all-sky satellite infrared radiances on convection-permitting analysis and prediction of tropical con-vection, Mon. Weather Rev., 148, 3203–3224, https://doi.org/10.1175/MWR-D-19-0343.1, 2020.
- Chandramouli, K., Wang, X., Johnson, A., and Otkin, J.: Online nonlinear bias correction in ensemble Kalman filter to assimilate GOES-R all-sky radiances for the analysis and prediction of rapidly developing supercells, Journal of Advances in Modeling Earth Systems, 14, e2021MS002711, https://doi.org/10.1029/2021MS002711, 2022.
- Cucurull, L., Derber, J. C., and Purser, R. J.: A bending angle forward operator for global positioning system radio occultation measurements, J. Geophys. Res.-Atmos., 118, 14–28, https://doi.org/10.1029/2012JD017782, 2013.
- Dee, D. P. and Uppala, S.: Variational bias correction of satellite radiance data in the ERA-Interim reanalysis, Q. J. Roy. Meteor. Soc., 135, 1830–1841, https://doi.org/10.1002/qj.493, 2009.
- Desroziers, G., Berre, L., Chapnik, B., and Poli, P.: Diagnosis of observation, background and analysis-error statistics in observation space, Q. J. R. Meteorol. Soc., 131, 3385–3396, https://doi.org/10.1256/qj.05.108, 2005.
- Evensen, G.: The Ensemble Kalman Filter: theoretical formulation and practical implementation, Ocean Dynam., 53, 343–367, https://doi.org/10.1007/s10236-003-0036-9, 2003.
- Fertig, E., Baek, S. J., Hunt, B., Ott, E., Szunyogh, I., Aravéquia, J., Kalnay, E., Li, H., and Liu, J.: Observation bias correction with an ensemble Kalman filter. Tellus A: Dynamic Meteorology and Oceanography, 61, 210–226, https://doi.org/10.1111/j.1600-0870.2008.00378.x, 2009.
- Frolov, S., Shlyaeva, A., Huang, W., Sluka, T., Draper, C., Huang, B., Martin, C., Elless, T., Bhargava, K., and Whitaker J.: Local volume solvers for Earth system data assimilation: Implementation in the framework for Joint Effort for Data Assimilation Integration, Journal of Advances in Modeling Earth Systems, 16, e2023MS003692, https://doi.org/10.1029/2023MS003692, 2024.

- Gaspari, G. and Cohn, S. E.: Construction of correlation functions in two and three dimensions, Q. J. R. Meteorol. Soc., 125, 723–757, https://doi.org/10.1002/qj.49712555417, 1999.
- Geer, A. J. and Bauer, P.: Observation errors in all-sky data assimilation, Q. J. R. Meteorol. Soc., 137, 2024–2037, https://doi.org/10.1002/qj.830, 2011
- Geer, A. J., Baordo, F., Bormann, N., Chambon, P., English, S. J., Kazumori, M., Lawrence, H., Lean, P., Lonitz, K., and Lupu, C.: The growing impact of satellite observations sensitive to humidity, cloud and precipitation, Q. J. R. Meteorol. Soc., 143, 3189– 3206, https://doi.org/10.1002/qj.3172, 2017.
- Geer, A. J., Lonitz, K., Weston, P., Kazumori, M., Okamoto, K., Zhu, Y., Liu, E. H., Collard, A., Bell, W., Migliorini, S., Chambon, P., Fourrié, N., Kim, M.-J., Köpken-Watts, C., and Schraff, C.: All-sky satellite data assimilation at operational weather forecasting centres, Q. J. R. Meteorol. Soc., 144, 1191–1217, https://doi.org/10.1002/qj.3202, 2018.
- Gilleland, E., Hering, A. S., Fowler, T. L., and Brown, B. G.: Testing the Tests: What Are the Impacts of Incorrect Assumptions When Applying Confidence Intervals or Hypothesis Tests to Compare Competing Forecasts?, Mon. Weather Rev., 146, 1685–1703, https://doi.org/10.1175/mwr-d-17-0295.1, 2018.
- Grody, N., Weng, F., and Ferraro, R.: Application of AMSU for obtaining water vapor, cloud liquid water, precipitation, snow cover and sea ice concentration. Preprints, 10th Int. TOVS Study Conf., Boulder, CO, Int. ATOVS Working Group, 230–240, https://pubs.ssec.wisc.edu/research_Resources/publications/ pdfs/ITSC10/grody01_ITSC10_1999.pdf (last access: 17 October 2025), 1999.
- Grody, N., Zhao, J., Ferraro, R., Weng, F., and Boers, R.: Determination of precipitable water and cloud liquid water over oceans from the NOAA 15 advanced microwave sounding unit, J. Geophys. Res., 106, 2943–2953, https://doi.org/10.1029/2000JD900616, 2001.
- Guerrette, J. J., Liu, Z., Snyder, C., Jung, B.-J., Schwartz, C. S.,
 Ban, J., Vahl, S., Wu, Y., Baños, I. H., Yu, Y. G., Ha, S., Trémolet, Y., Auligné, T., Gas, C., Ménétrier, B., Shlyaeva, A., Miesch, M., Herbener, S., Liu, E., Holdaway, D., and Johnson, B. T.: Data assimilation for the Model for Prediction Across Scales Atmosphere with the Joint Effort for Data assimilation Integration (JEDI-MPAS 2.0.0-beta): ensemble of 3D ensemblevariational (En-3DEnVar) assimilations, Geosci. Model Dev., 16, 7123–7142, https://doi.org/10.5194/gmd-16-7123-2023, 2023.
- Ha, S., Snyder, C., Skamarock, W. C., Anderson, J. L., and Collins, N.: Ensemble Kalman filter data assimilation for the Model for Prediction Across Scales (MPAS), Mon. Weather Rev., 145, 4673–4692, https://doi.org/10.1175/MWR-D-17-0145.1, 2017.
- Healy, S. B. and Thépaut, J. N.: Assimilation experiments with CHAMP GPS radio occultation measurements, Q. J. R. Meteorol. Soc., 132, 605–623, https://doi.org/10.1256/qj.04.182, 2006.
- Honda, T., Miyoshi, T., Lien, G., Nishizawa, S., Yoshida, R., Adachi, S. A., Terasaki, K., Okamoto, K., Tomita, H., and Bessho, K.: Assimilating All-Sky Himawari-8 Satellite Infrared Radiances: A Case of Typhoon Soudelor (2015), Mon. Weather Rev., 146, 213–229, https://doi.org/10.1175/MWR-D-16-0357.1, 2018.
- Houtekamer, P. L., Lefaivre, L., Derome, J., Ritchie, H., and Mitchell, H. L.: A system simulation approach to ensemble prediction, Mon. Weather

- Rev., 124, 1225–1242, https://doi.org/10.1175/1520-0493(1996)124<1225:ASSATE>2.0.CO;2, 1996.
- Hunt, B. R., Kostelich, E. J., and Szunyogh. I.: Efficient data assimilation for spatiotemporal chaos: A local ensemble transform Kalman filter, Physica D: Nonlinear Phenomena, 230, 112–126, https://doi.org/10.1016/j.physd.2006.11.008, 2007.
- Ingleby, B.: Global assimilation of air temperature, humidity, wind and pressure from surface stations, Q. J. Roy. Meteor. Soc., 141, 504–517, https://doi.org/10.1002/qj.2372, 2014.
- Johnson, B. T., Dang, C., Stegmann, P., Liu, Q., Moradi, I., and Auligne, T.: The Community Radiative Transfer Model (CRTM): Community-Focused Collaborative Model Development Accelerating Research to Operations, Bull. Amer. Meteor. Soc., 104, E1817–E1830, https://doi.org/10.1175/BAMS-D-22-0015.1, 2023.
- Joint Center for Satellite Data Assimilation and National Center for Atmospheric Research: JEDI-MPAS Data Assimilation System v2.1.0 (2.1.0), Zenodo [code], https://doi.org/10.5281/zenodo.15201032, 2023.
- Jung, B.-J., Ménétrier, B., Snyder, C., Liu, Z., Guerrette, J. J., Ban, J., Baños, I. H., Yu, Y. G., and Skamarock, W. C.: Threedimensional variational assimilation with a multivariate background error covariance for the Model for Prediction Across Scales – Atmosphere with the Joint Effort for Data assimilation Integration (JEDI-MPAS 2.0.0-beta), Geosci. Model Dev., 17, 3879–3895, https://doi.org/10.5194/gmd-17-3879-2024, 2024.
- Kalnay, E., Ota, Y., Miyoshi, T., and Liu, J.: A simpler formulation of forecast sensitivity to observations: Application to ensemble Kalman filters, Tellus, 64A, 18462, https://doi.org/10.3402/tellusa.v64i0.18462, 2012
- Kotsuki, S., Ota, Y., and Miyoshi, T.: Adaptive covariance relaxation methods for ensemble data assimilation: experiments in the real atmosphere, Q. J. R. Meteorol. Soc., 143, 2001–2015, https://doi.org/10.1002/qj.3060, 2017.
- Lei, L., Whitaker, J. S., and Bishop, C.: Improving assimilation of radiance observations by implementing model space localization in an ensemble Kalman filter, Journal of Advances in Modeling Earth Systems, 10, 3221–3232, https://doi.org/10.1029/2018MS001468, 2018.
- Lei, L., Whitaker, J. S., Anderson, J. L., and Tan, Z.: Adaptive localization for satellite radiance observations in an ensemble Kalman filter, Journal of Advances in Modeling Earth Systems, 12, e2019MS001693, https://doi.org/10.1029/2019MS001693, 2020
- Liu, J. and Kalnay, E.: Estimating observation impact without adjoint model in an ensemble Kalman filter, Q. J. Roy. Meteor. Soc., 134, 1327–1335, https://doi.org/10.1002/qj.280, 2008.
- Liu, Z., Snyder, C., Guerrette, J. J., Jung, B.-J., Ban, J., Vahl, S., Wu, Y., Trémolet, Y., Auligné, T., Ménétrier, B., Shlyaeva, A., Herbener, S., Liu, E., Holdaway, D., and Johnson, B. T.: Data assimilation for the Model for Prediction Across Scales Atmosphere with the Joint Effort for Data assimilation Integration (JEDI-MPAS 1.0.0): EnVar implementation and evaluation, Geosci. Model Dev., 15, 7859–7878, https://doi.org/10.5194/gmd-15-7859-2022, 2022.
- Lonitz, K. and Geer, A. J.: New screening of cold-air outbreak regions used in 4D-Var all-sky assimilation. Technical Report 35, EUMETSAT/ECMWF Fellowship Programme Research Report Shinfield Park, Reading, https://www.ecmwf.int/node/ 10777 (last access: 17 October 2025), 2015.

- Migliorini, S. and Candy, B.: All-sky satellite data assimilation of microwave temperature sounding channels at the Met Office, Q. J. Roy. Meteor. Soc., 145, 867–883,https://doi.org/10.1002/qj.3470, 2019.
- Minamide, M. and Zhang, F.: Assimilation of All-Sky Infrared Radiances from Himawari-8 and Impacts of Moisture and Hydrometer Initialization on Convection-Permitting Tropical Cyclone Prediction, Mon. Weather Rev., 146, 3241–3258, https://doi.org/10.1175/MWR-D-17-0367.1, 2018.
- Miyoshi, T., Sato, Y., and Kadowaki, T.: Ensemble Kalman filter and 4D-Var intercomparison with the Japanese operational global analysis and prediction system, Mon. Weather Rev., 138, 2846–2866, https://doi.org/10.1175/2010mwr3209.1, 2010.
- NASA: Goddard Earth Sciences Data and Information Services Center (GES DISC) OPeNDAP data access portal, NASA Goddard Space Flight Center [data set], https://sounder.gesdisc. eosdis.nasa.gov/opendap, last access: 17 October 2025.
- National Centers for Environmental Prediction/National Weather Service/NOAA/U.S. Department of Commerce: NCEP ADP Global Upper Air and Surface Weather Observations (PREP-BUFR format), Research Data Archive at the National Center for Atmospheric Research, Computational and Information Systems Laboratory [data set], https://doi.org/10.5065/Z83F-N512, 2008.
- National Centers for Environmental Prediction/National Weather Service/NOAA/U.S. Department of Commerce: NCEP GDAS Satellite Data 2004–continuing, Research Data Archive at the National Center for Atmospheric Research, Computational and Information Systems Laboratory [data set], https://doi.org/10.5065/DWYZ-Q852, 2009.
- National Centers for Environmental Prediction/National Weather Service/NOAA/U.S. Department of Commerce: NCEP GFS 0.25 Degree Global Forecast Grids Historical Archive, Research Data Archive at the National Center for Atmospheric Research, Computational and Information Systems Laboratory [data set], https://doi.org/10.5065/D65D8PWK, 2015.
- Nerger, L.: On serial observation processing in localized ensemble Kalman filters, Mon. Weather Rev., 143, 1554–1567, https://doi.org/10.1175/MWR-D-14-00182.1, 2015.
- NOAA: Global Ensemble Forecast System (GEFS), NOAA [data set], https://www.ncei.noaa.gov/products/weather-climate-models/global-ensemble-forecast, last access: 17 October 2025.
- Okamoto, K., Sawada, Y., and Kunii, M.: Comparison of assimilating all-sky and clear-sky infrared radiances from Himawari-8 in a mesoscale system, Q. J. R. Meteorol. Soc., 145, 745–766, https://doi.org/10.1002/qj.3463, 2019.
- Okamoto, K., Ishibashi, T., and Okabe, I.: All-sky infrared radiance assimilation of a geostationary satellite in the Japan Meteorological Agency's global system, Q. J. R. Meteorol. Soc., 149, 2477–2503, https://doi.org/10.1002/qj.4516, 2023.
- Park, J., Xue, M., and Liu, C.: Implementation and testing of radar data assimilation capabilities within the Joint Effort for Data Assimilation Integration framework with ensemble transformation Kalman filter coupled with FV3-LAM model, Geophysical Research Letters, 50, e2022GL102709, https://doi.org/10.1029/2022GL102709, 2023.
- Rennie, M. P.: The impact of GPS radio occultation assimilation at the Met Office, Q. J. R. Meteorol. Soc., 136, 116–131, https://doi.org/10.1002/qj.521, 2010.

- Shahabadi, M. B. and Buehner, M.: Implementation of All-Sky Assimilation of Microwave Humidity Sounding Channels in Environment Canada's Global Deterministic Weather Prediction System, Mon. Wea. Rev., 152, 1027–1038, https://doi.org/10.1175/MWR-D-23-0227.1, 2024.
- Shao, H., Derber, J., Huang, X.-Y., Hu, M., Newman, K., Stark, D., Lueken, M., Zhou, C., Nance, L., Kuo, Y.-H., and Brown, B.: Bridging research to operations transitions: Status and plans of community GSI, Bull. Amer. Meteor. Soc., 97, 1427–1440, https://doi.org/10.1175/BAMS-D-13-00245.1, 2016.
- Skamarock, W. C., Klemp, J. B., Duda, M. G., Fowler, L. D., Park, S.-H., and Ringler, T. D.: A Multiscale Nonhydrostatic Atmospheric Model Using Centroidal Voronoi Tessellations and C-Grid Staggering, Mon. Weather Rev., 140, 3090–3105, https://doi.org/10.1175/mwrd-11-00215.1, 2012.
- Skamarock, W. C., Duda, M. G., Ha, S., and Park, S.-H.: Limited-Area Atmospheric Modeling Using an Unstructured Mesh, Mon. Weather Rev., 146, 3445–3460, https://doi.org/10.1175/mwr-d-18-0155.1, 2018.
- Tippett, M. K., Anderson, J. L., Bishop, C. H., Hamill, T. M., and Whitaker, J. S.: Ensemble Square Root Filters, Mon. Weather Rev., 131, 1485–1490, https://doi.org/10.1175/1520-0493(2003)131<1485:ESRF>2.0.CO;2, 2003.
- Tong, M., Zhu, Y., Zhou, L., Liu, E., Chen, M., Liu, Q., and Lin, S.: Multiple Hydrometeors All-Sky Microwave Radiance Assimilation in FV3GFS, Mon. Weather Rev., 148, 2971–2995, https://doi.org/10.1175/MWR-D-19-0231.1, 2020.
- Trémolet, Y. and Auligné T.: The Joint Effort for Data Assimilation Integration (JEDI), JCSDA Quarterly Newsletter, 66, 1–5, https://doi.org/10.25923/RB19-0Q26, 2020.
- Wang, X., Chipilski, H. G., Bishop, C. H., Satterfield, E., Baker, N., and Whitaker, J. S.: A Multiscale Local Gain Form Ensemble Transform Kalman Filter (MLGETKF), Mon. Weather Rev., 149, 605–622, https://doi.org/10.1175/MWR-D-20-0290.1, 2021.
- Weston, P., Geer, A. J., and Bormann, N.: Investigations into the assimilation of AMSU-A in the presence of cloud and precipitation. Technical Report 50, EUMET-SAT/ECMWF Fellowship Programme Research Report, https://doi.org/10.21957/ewahn9ce, 2019.
- Whitaker, J. S. and Hamill, T. M.: Ensemble data assimilation without perturbed observations, Mon. Weather Rev., 130, 1913–1924, https://doi.org/10.1175/1520-0493(2002)130<1913:EDAWPO>2.0.CO;2, 2002.
- Whitaker, J. S. and Hamill, T. M.: Evaluating Methods to Account for System Errors in Ensemble Data Assimilation, Mon. Weather Rev., 140, 3078–3089, https://doi.org/10.1175/MWR-D-11-00276.1, 2012.
- Zhang, F., Snyder, C., and Sun, J.: Impacts of Initial Estimate and Observation Availability on Convective-Scale Data Assimilation with an Ensemble Kalman Filter. Mon. Weather Rev., 132, 1238–1253, https://doi.org/10.1175/1520-0493(2004)132<1238:IOIEAO>2.0.CO;2, 2004.
- Zhang, F., Minamide, M., and Clothiaux, E. E.: Potential impacts of assimilating all-sky infrared satellite radiances from GOES-R on convection-permitting analysis and prediction of tropical cyclones, Geophys. Res. Lett., 43, 2954–2963, https://doi.org/10.1002/2016GL068468, 2016.
- Zhang, F., Minamide, M., Nystrom, R. G., Chen, X., Lin, S.-J., and Harris, L. M.: Improving Harvey forecasts with next-generation

- weather satellites: Advanced hurricane analysis and prediction with assimilation of GOES-R all-sky radiances, Bull. Amer. Meteor. Soc., 100, 1217–1222, https://doi.org/10.1175/BAMS-D-18-0149.1, 2019.
- Zhu, L., Xue, M., Kong, R., and Min, J.: Direct Assimilation of All-Sky GOES-R ABI Radiances in GSI EnKF for the Analysis and Forecasting of a Mesoscale Convective System, Mon. Weather Rev., 151, 737–760, https://doi.org/10.1175/MWR-D-21-0293.1, 2023
- Zhu, Y., Liu, E., Mahajan, R., Thomas, C., Groff, D., Delst,
 P. V., Collard, A., Kleist, D., Treadon, R., and Derber, J.
 C.: All-Sky Microwave Radiance Assimilation in the NCEP's
 GSI Analysis System, Mon. Weather Rev., 144, 4709–4735,
 https://doi.org/10.1175/MWR-D-15-0445.1, 2016.
- Zhu, Y., Gayno, G., Purser, R. J., Su, X., and Yang, R.: Expansion of the All-Sky Radiance Assimilation to ATMS at NCEP, Mon. Weather Rev., 147, 2603–2620, https://doi.org/10.1175/MWR-D-18-0228.1, 2019.